NANO LETTERS

pubs.acs.org/NanoLett Letter

Magnetic Amplification at Yb^{3+} "Designer Defects" in the van der Waals Ferromagnet CrI_3

Kimo Pressler, Thom J. Snoeren, Kelly M. Walsh, and Daniel R. Gamelin*

Cite This: *Nano Lett.* 2023, 23, 1320−1326 Read Online

ABSTRACT: The two-dimensional (2D) van der Waals ferromagnet CrI_3 has been doped with the magnetic optical impurity Yb^{3+} to yield materials that display sharp multiline Yb^{3+} photoluminescence (PL) controlled by the magnetism of CrI_3. Magneto-PL shows that Yb^{3+} magnetization is pinned to the magnetization of CrI_3. An effective internal field of ∼10 T at Yb^{3+} is estimated, attributed to strong in-plane Yb^{3+}−Cr^{3+} superexchange coupling. The anomalously low energy of Yb^{3+} PL in CrI_3 reflects relatively high Yb^{3+}−I^- covalency, contributing to Yb^{3+}−Cr^{3+} superexchange coupling. The Yb^{3+} PL energy and line width both reveal the effects of spontaneous zero-field CrI_3 magnetic ordering *within* 2D layers below T_C, despite the absence of net magnetization in multilayer samples. These results illustrate the use of optical impurities as "designer defects" to introduce unique functionality to 2D magnets.

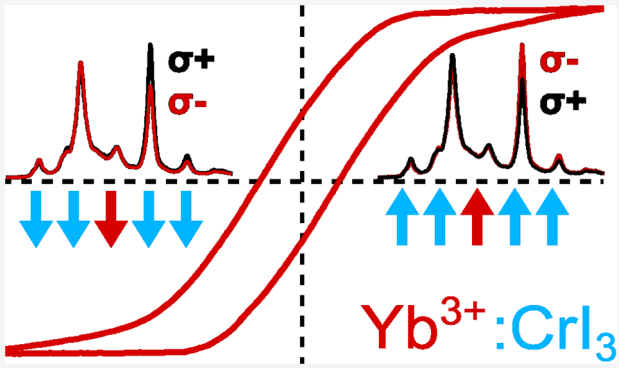

KEYWORDS: *2D ferromagnet, lanthanide doping, molecular field, chromium triiodide, photoluminescence*

Defects have the power to transform the physical properties of crystals, imparting new and potentially useful functionalities from conductivity to quantum photon emission.[1−6] In magnetic materials, defects can strongly affect spin-wave propagation, magnetic domain-wall propagation, skyrmion dynamics, and magnetic vortex pinning.[7−9] Recently, the layered van der Waals ferromagnet CrI_3 has emerged as a promising platform for exploring strongly correlated spin physics, magnetic proximity effects, and next-generation spin-based device architectures in the two-dimensional (2D) limit,[10−14] but the potential to expand CrI_3 functionality through the introduction of defects remains untapped. Here, we report that doping CrI_3 with Yb^{3+} as a "designer point defect" transforms its normally broad and featureless d−d photoluminescence (PL) into narrow-line sensitized f−f emission, without compromising its attractive magnetic properties. We further show that Yb^{3+} in CrI_3 experiences a large internal effective field that makes it extremely sensitive to small external magnetic fields. Using this property, we demonstrate magnetically saturated circular polarization of Yb^{3+} emission at anomalously small applied fields. Strikingly, the internal effective field also transmits magnetic information to Yb^{3+} even in the absence of any applied field, making Yb^{3+} a unique embedded luminescent probe of spontaneous zero-field magnetic ordering within the 2D monolayers of bulk CrI_3. These discoveries establish optical impurity doping as an effective strategy for expanding the functionality of 2D magnets, with potential ramifications for both basic science and future spin-photonic technologies.

CrI_3 has become a model system for exploring magnetic exchange in 2D van der Waals structures,[10−14] stimulated by recent discoveries of Ising-like hard ferromagnetism in exfoliated monolayer CrI_3 and layer- and stacking-dependent magnetism in multilayer CrI_3.[15,16] Layering CrI_3 with nonmagnetic 2D materials introduces magnetic functionality to the nonmagnetic material via interlayer exchange coupling, allowing magnetic manipulation of properties such as WSe_2 valley polarization and valley Zeeman splittings.[17] Extension from few to many (bulk) layers preserves the strong Ising-like intralayer ferromagnetic ordering, but facile motion of domain walls unblocks demagnetization.[18] Despite its rich magnetic properties, CrI_3 itself has not garnered much attention as an optical material. Bulk CrI_3 has been investigated for its very large Kerr and Faraday rotation strengths in relation to optical isolators and associated technologies.[19,20] PL of bulk CrI_3 has apparently not been reported, and few-layer CrI_3 shows[17] only the very broad d−d PL characteristic of weak-field pseudo-octahedral Cr^{3+}.[21] Circular polarization of this d−d PL was used to probe the magnetism of few-layer CrI_3,[17] but the emission's breadth limits its further utility for fundamental

Received: November 17, 2022
Revised: January 29, 2023
Published: February 1, 2023

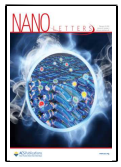

https://doi.org/10.1021/acs.nanolett.2c04533
Nano Lett. 2023, 23, 1320−1326

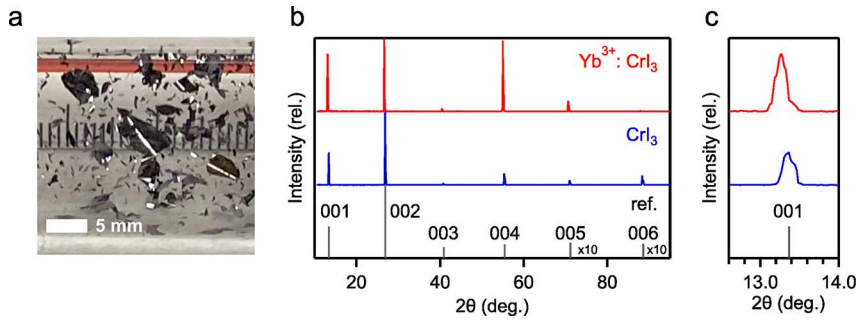

Figure 1. (a) Photograph of 4.9% Yb^{3+}:CrI_3 crystals prepared by chemical vapor transport. The scale bar indicates 5 mm. All experiments were performed on individual single-crystal flakes from such a reaction tube. (b) XRD data collected on undoped and Yb^{3+}-doped CrI_3 single crystals using a powder diffractometer. Only (00*l*) peaks are observed, indicating an oriented sample. Reference peaks for *c*-oriented CrI_3 diffraction are included (black, ICSD Coll. Code 251654). (c) Magnified view of the 001 reflection for the same samples, displaying an increase in the interlayer lattice spacing upon Yb^{3+} doping. The *x* axis in (c) was determined as described in the Supporting Information.

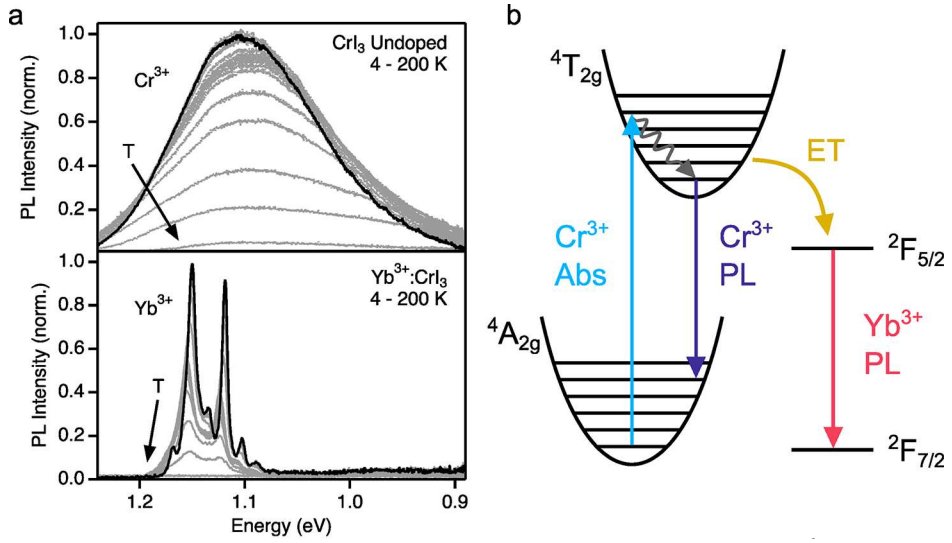

Figure 2. (a) Variable-temperature PL spectra of CrI_3 (top) and 4.9% Yb^{3+}:CrI_3 (bottom), measured from 4 to 200 K under 1.88 eV CW excitation at 4 mW/cm^2. (b) Single-configurational-coordinate diagram (A_{1g} coordinate) describing vibronic broadening of the absorption and luminescence bands associated with transitions between the $^4A_{2g}$ and $^4T_{2g}$ ligand-field states of pseudo-octahedral Cr^{3+}. In Yb^{3+}-doped CrI_3, energy transfer from the Cr^{3+} $^4T_{2g}$ excited state to Yb^{3+} yields sensitized $^2F_{5/2} \rightarrow {}^2F_{7/2}$ f−f luminescence.

studies or in spin-photonics, stimulating efforts to narrow the band via cavity coupling.[22] Doping CrI_3 with optically active impurities has also not been reported, in either bulk or exfoliated samples.

To investigate *intra*layer "proximity" effects resulting from magnetic exchange coupling, we have prepared CrI_3 doped with luminescent and spin-bearing Yb^{3+} ions. Large-diameter single-crystal flakes of CrI_3 were prepared by chemical vapor transport. Yb^{3+} was introduced by adding Yb(0) to the precursor mix. The Yb^{3+} concentration in the resulting Yb^{3+}:CrI_3 crystals is controllable, and samples with up to ∼5% Yb^{3+} (cation mole fraction, $[Yb^{3+}]/([Cr^{3+}] + [Yb^{3+}])$) are described here. Further experimental details are provided in the Supporting Information. Figure 1a shows a photograph of representative Yb^{3+}:CrI_3 flakes in their growth tube. The flakes are between 5 and 10 mm across, with typical thicknesses of 5−20 μm (see the Supporting Information). Figure 1b plots XRD data collected on undoped and 4.9% Yb^{3+}-doped CrI_3 single-crystal flakes using a powder diffractometer. Only (00*l*) peaks are observed, corresponding to the interlayer lattice spacing and reflecting the flake's alignment. Figure 1c highlights the shift to smaller angle of the 001 peak upon doping. From fitting the XRD peak positions of undoped and 4.9% Yb^{3+}-doped CrI_3 samples, the interlayer lattice parameter was found to increase 0.24% from 6.996 ± 0.002 to 7.013 ± 0.002 Å, attributed to the larger ionic radius of Yb^{3+} than of Cr^{3+} (87 vs 62 pm, respectively) (see the Supporting Information). These data suggest that the local strain of doping is relieved by distorting the lattice along its softest dimension, as expected. Substitutional incorporation of Yb^{3+} at the Cr^{3+} site is verified by single-crystal XRD measurements (see the Supporting Information), which also show the increased interlayer spacing. The single-crystal data show no detectable electron density between layers, ruling out Yb^{3+} intercalation.

Figure 2a plots the PL spectra of CrI_3 and Yb^{3+}:CrI_3 single flakes measured at several temperatures between 4 and 200 K. The CrI_3 spectrum broadens and decreases in intensity with increasing temperature, eventually reaching only 7.5% of its 4 K intensity at 200 K (see the Supporting Information). Although the broadening to higher energies is expected from thermal hot bands, the broadening to lower energies is abnormal and suggests an additional feature. Upon introduction of Yb^{3+}, the broad featureless d−d emission of Cr^{3+}

https://doi.org/10.1021/acs.nanolett.2c04533
Nano Lett. 2023, 23, 1320−1326

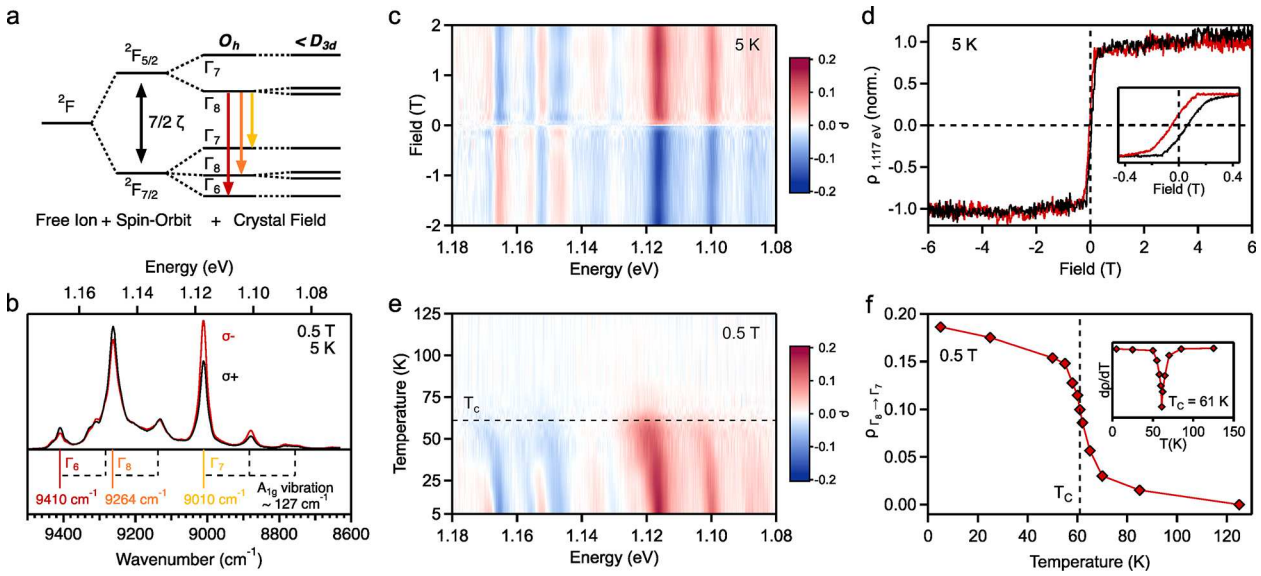

Figure 3. (a) Splitting of the Yb^{3+} free-ion ^2F term due to spin−orbit (ζ) and crystal-field (O_h, $<D_{3d}$) interactions. The colored down arrows indicate the three crystal-field transitions anticipated in the low-temperature PL spectrum in the idealized O_h site symmetry. The actual site symmetry is reduced to $<D_{3d}$, e.g., to C_2, splitting each Γ_8 level into two Kramers doublets. (b) Magnetic circularly polarized luminescence (MCPL) spectra of 4.9% Yb^{3+}:CrI_3 measured at 5 K with an applied magnetic field of 0.5 T. The σ^- (red) and σ^+ (black) spectra were collected using unpolarized 1.88 eV CW excitation at 40 mW/cm^2 and have different amplitudes. The three electronic origins in idealized O_h symmetry are indicated below the spectra, assigned to the $\Gamma_8 \to \Gamma_6$, Γ_8, and Γ_7 transitions illustrated in (a). The dashed black lines indicate vibronic sidebands with a characteristic energy spacing of ∼127 cm^{-1} (15.7 meV), consistent with the A_{1g} lattice mode of CrI_3. (c) False-color plot of the MCPL polarization ratio, $\rho = (\sigma^- - \sigma^+)/(\sigma^- + \sigma^+)$, for the full Yb^{3+} PL spectrum, measured from −2 to +2 T at 5 K. (d) Polarization ratio of the $\Gamma_8 \to \Gamma_7$ electronic origin (1.117 eV) plotted as a function of magnetic field from −6 to 6 T. The black (red) trace corresponds to the positive (negative) field sweep direction. Inset: expanded plot of ρ between −0.4 and +0.4 T, showing a coercive field of ∼55 mT. The sample was excited with linearly polarized 1.96 eV excitation (see Experimental Methods in the Supporting Information). (e) False-color plot of the polarization ratio vs temperature, measured at 0.5 T. The dashed black line indicates the Curie temperature of bulk CrI_3 (T_C = 61 K). (f) Plot of the $\Gamma_8 \to \Gamma_7$ polarization ratio at the peak maximum measured at 0.5 T as a function of temperature. The red curve is a guide to the eye. Inset: derivative of ρ as a function of temperature. The extracted Curie temperature is 61 K, indistinguishable from that of the undoped crystal.

disappears and is replaced by a series of sharp f−f transitions of Yb^{3+} around 1.15 eV. An assignment of the PL fine structure is discussed later. In some samples, Yb^{3+} doping also reveals another broad emission band centered at ∼0.95 eV, which is responsible for the red tail of the CrI_3 PL here and in some literature spectra. This feature has been traced to Ni^{2+} impurities (<0.4%) found in some Cr(0) precursors, and it can be mostly eliminated by using 5N Cr(0) precursors (Figure 2a, bottom). The Yb^{3+} PL is not influenced by this Ni^{2+} impurity (see the Supporting Information).

Figure 2b illustrates the photophysics of Yb^{3+}:CrI_3 schematically. The lowest-energy excited state of CrI_3 is the Cr^{3+} $^4T_{2g}$ ligand-field state, involving excitation of a t_{2g} electron into a σ-antibonding e_g orbital (in idealized O_h symmetry). The resulting change in equilibrium geometry is described by the single-configurational-coordinate (SCC) diagram of Figure 2b, which illustrates the totally symmetric distortion coordinate. This $^4T_{2g}$ excited state also distorts along a symmetry-breaking Jahn−Teller coordinate (not illustrated).[21] These distortions lead to extensive vibronic progressions in the absorption and PL spectra associated with this transition and cause a large PL Stokes shift. Doping CrI_3 with Yb^{3+} introduces a set of $^2F_{5/2}$ states just below the Cr^{3+} $^4T_{2g}$ excited state, favorably positioned for efficient $Cr^{3+} \to Yb^{3+}$ energy transfer. At 4.9% Yb^{3+} doping, the Cr^{3+} $^4T_{2g}$ PL is entirely quenched and strong Yb^{3+} $^2F_{5/2}$ emission is observed in its place (Figure 2a). Because both Cr^{3+} and Yb^{3+} states are localized at single ions, energy migration within the CrI_3 lattice is required for this complete quenching. In undoped CrI_3, energy migration among equivalent Cr^{3+} sites may occur but is not readily apparent. In Yb^{3+}:CrI_3, this energy migration is interrupted when energy is captured by Yb^{3+} dopants. In 4.9% Yb^{3+}:CrI_3, the average Cr^{3+} ion has only ∼14% probability of having a neighboring Yb^{3+} and ∼50% probability of having at least one Yb^{3+} within its first two cation shells. Energy must therefore migrate over at least a few lattice sites within the $^4T_{2g}$ lifetime to fully quench the Cr^{3+} emission as observed in Figure 2a.

Figure 3a shows the anticipated electronic structure of Yb^{3+} in CrI_3. In the free ion, spin−orbit coupling splits the ^2F term into $^2F_{5/2}$ (excited) and $^2F_{7/2}$ (ground) states by the amount $\Delta E = 7/2\zeta$, where ζ = 361.8 meV is the free-ion spin−orbit coupling constant.[23] In crystals, each of these states is further split by the crystal field. Figure 3b shows circularly polarized PL spectra of 4.9% Yb^{3+}:CrI_3 measured in a 0.5 T field applied parallel to the crystal's *c* axis (*vide infra*). Three zero-phonon electronic origins are observed and assigned to the $\Gamma_8 \to \Gamma_6$, Γ_8, and Γ_7 transitions anticipated from Figure 3a using idealized O_h notation. The actual cation site symmetry in CrI_3 is lower (Figure 3a, right),[24] but the expected low-symmetry splitting of the Γ_8 origin is not clearly identifiable. The Γ_6 peak is broad with observable structure on its high-energy shoulder, thus making the precise energy of this origin unclear within ∼20 cm^{-1} (∼2.5 meV). An analysis of these PL energies within the angular overlap model (AOM)[25] reproduces the $^2F_{7/2}$ splittings well, predicting a $^2F_{5/2}$ splitting of ∼34 meV and splittings of the two Γ_8 levels by <0.5 meV each (see the Supporting Information). Additional satellite features are observed ∼127 cm^{-1} (15.7 meV) below the Γ_8 and Γ_7

https://doi.org/10.1021/acs.nanolett.2c04533
Nano Lett. 2023, 23, 1320−1326

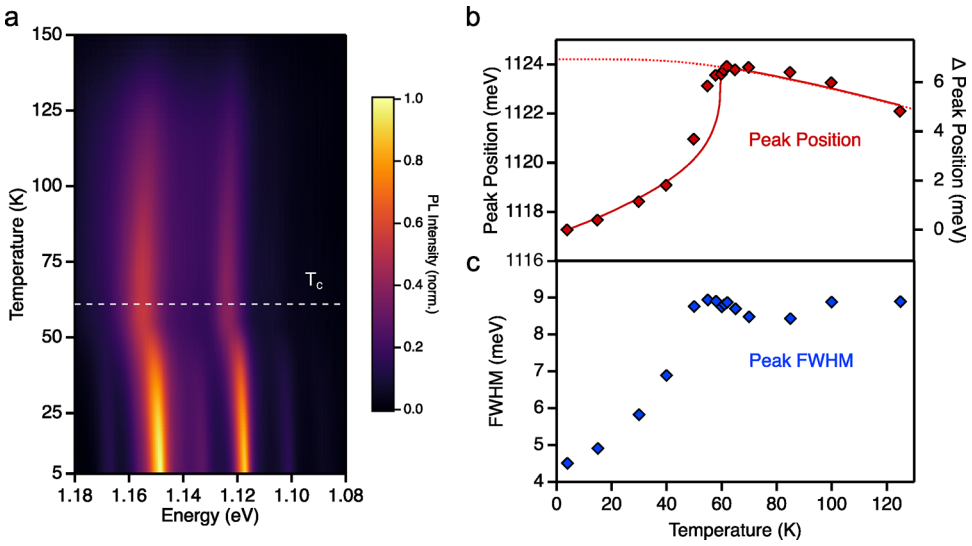

Figure 4. (a) False-color plot of the Yb^{3+} PL intensities vs temperature measured for 4.9% Yb^{3+}:CrI_3 from 4 to 150 K at zero external magnetic field. The horizontal dashed line indicates T_C = 61 K. (b) Peak position of the $\Gamma_8 \rightarrow \Gamma_7$ transition plotted vs temperature. The solid red curve shows the behavior predicted from the combination of resonant phonon interactions (eq 4) and spontaneous magnetization (below T_C, eq 6). The dashed red curve shows the behavior predicted from eq 4 alone below T_C. The solid curve was obtained using eqs 4 and 6 with fixed parameters of Δ = 127 cm^{-1} (15.7 meV), T_C = 60 K, and β = 1/3, adjusting only the amplitude scaling. (c) Plot of the $\Gamma_8 \rightarrow \Gamma_7$ PL line width vs temperature, from the same VTPL measurements.

electronic origins and assigned as phonon sidebands. Raman spectra show a totally symmetric lattice breathing mode of CrI_3 at this energy (ν = 127 cm^{-1}).[26]

A striking aspect of this Yb^{3+}:CrI_3 PL is its very low energy relative to other reported Yb^{3+} PL. This energy is primarily determined by spin−orbit coupling (Figure 3a). Yb^{3+} spin−orbit coupling can be reduced from that in the free ion by covalent expansion of the f-electron wave functions (nephelauxetic effect),[27,28] but f-orbital covalency in trivalent lanthanides is typically very small and this effect is usually considered negligible at ambient pressure. A survey of Yb^{3+}-doped crystals shows that the energy gap between Yb^{3+} $^2F_{5/2}$ and $^2F_{7/2}$ barycenters remains very near the free-ion value of $\Delta E \approx$ 1.266 eV across doped oxide, fluoride, chloride, bromide, sulfide, and phosphide lattices (see the Supporting Information).[29−33] We note that we have been unable to find *any* reports of PL from other Yb^{3+}-doped iodide crystals, perhaps because Yb^{3+} is easily reduced to Yb^{2+} under common iodide crystal-growth conditions. Yb^{3+}:CrI_3 deviates from this typical behavior substantially: ΔE is only ∼1.163 eV, or ∼9% smaller than in the free ion, representing the smallest spin−orbit coupling yet reported for Yb^{3+}. Covalency in Yb^{3+}:CrI_3 is certainly enhanced by the large ionic radius and polarizability of the iodides, but this consideration alone likely cannot explain the anomaly. The atomic spin−orbit coupling of I is also much greater than those of other common ligands for Yb^{3+} and should contribute to the spectroscopic spin−orbit splitting via covalency. Furthermore, the large ionic radius of Yb^{3+} compared to Cr^{3+} means that Yb^{3+} experiences an internal pressure imposed by the surrounding lattice, which may also increase covalency. Importantly, Yb^{3+}−I^- covalency is essential for strong Yb^{3+}−Cr^{3+} superexchange coupling.

From Figure 3a, all features show circularly polarized PL, with the $\Gamma_8 \rightarrow \Gamma_7$ origin showing the greatest polarization ratio ($\rho = (\sigma^- - \sigma^+)/(\sigma^- + \sigma^+)$ = 19%). ρ is independent of excitation power, but its maximum value varies somewhat between samples (see the Supporting Information). Figure 3c plots ρ across the entire PL spectrum as a function of magnetic field. All Yb^{3+} transitions are influenced by the applied field in the same way, consistent with all PL arising from the same excited state (Γ_8). Figure 3d plots ρ for the $\Gamma_8 \rightarrow \Gamma_7$ peak as a function of applied field. ρ increases rapidly at very low fields and saturates at only ∼0.2 T. Increasing the field from 0.2 to 6.0 T does not change ρ further, consistent with complete magnetization of Yb^{3+} by 0.2 T. On an expanded scale, these data show a hysteresis with a coercivity of ∼55 mT, comparable to that found in magnetic measurements of bulk CrI_3.[18,34] We note that these ρ values are generally small compared to those in cubic Yb^{3+}:InP (∼70% at 10 T, 4.2 K),[33] possibly suggesting an in-plane or canted Yb^{3+} anisotropy. Figure 3e summarizes the temperature dependence of ρ, measured at 0.5 T, and Figure 3f highlights the temperature dependence for $\Gamma_8 \rightarrow \Gamma_7$ individually. All spectral features behave similarly, showing a pronounced drop in polarization at the Curie temperature of bulk CrI_3 (∼61 K; see Figure 3f, inset). These magneto-optical data agree well with magnetic susceptibility data (see the Supporting Information), and both indicate that Yb^{3+} doping causes no significant change in the magnetic characteristics of CrI_3 in these samples. This MCPL field and temperature dependence is highly unusual for Yb^{3+}, which generally shows simple paramagnetism of a pseudospin 1/2. For example, our AOM crystal-field analysis (see the Supporting Information) predicts $g_{avg} \approx$ 2.7 for the lowest $^2F_{7/2}$ Kramers doublet. Overall, the anomalous magnetism seen in the Yb^{3+} MCPL reflects *magnetic* integration of Yb^{3+} with ferromagnetic CrI_3.

Magnetic ordering was originally explained by Weiss in terms of a huge internal "molecular field"[35] exerted upon individual ions by their surrounding magnetic matrix, and this model provides a useful heuristic for estimating the effective field experienced by Yb^{3+} within CrI_3. In this model, the effective field is given by the sum of external and molecular fields, as in eq 1.

$$H_{eff} = H_{ext} + H_{mol} \quad (1)$$

https://doi.org/10.1021/acs.nanolett.2c04533
Nano Lett. 2023, 23, 1320−1326

In Figure 3c,d, CrI_3 reaches magnetic saturation at very small H_{ext} (<0.2 T). At such low fields, $H_{ext} \ll H_{mol}$, and hence $H_{eff} \approx H_{mol}$. In the molecular-field model, H_{mol} in CrI_3 is given by eq 2

$$H_{mol} = \frac{2zJ\langle S\rangle}{g\mu_B} \tag{2}$$

where J is the nearest-neighbor exchange coupling constant, $z = 3$ in CrI_3, g is the Landé g factor (2.00 for Cr^{3+} in CrI_3), μ_B is the Bohr magneton, and $\langle S\rangle$ is the spin expectation value for Cr^{3+} in CrI_3, whose absolute value equals 3/2 at saturation. T_C in this model is determined by J according to eq 3

$$T_C = \frac{2zJS(S+1)}{3k_B} \tag{3}$$

where $S = 3/2$ for Cr^{3+} and k_B is the Boltzmann constant. From $T_C = 61$ K, eq 3 yields a value of $J = 0.70$ meV in CrI_3. Entering this J value into eq 2 yields $H_{mol} \approx 54$ T in CrI_3. H_{mol} is dominated by superexchange coupling, since dipolar contributions cannot account for the high T_C of CrI_3.[36] For Yb^{3+} in CrI_3, J is reduced by the shielding of the 4f orbitals. Cr^{3+}(d)−Yb^{3+}(f) superexchange coupling has received relatively little experimental or theoretical attention,[37−39] but relevant experimental data are found in inelastic neutron scattering analyses of $Cs_3Yb_{1.8}Cr_{0.2}Br_9$, where Yb^{3+}−Cr^{3+} exchange splittings are ∼1/4 those for Cr^{3+}−Cr^{3+}.[37] This scaling factor is approximate because of the different lattice structure, but $Cs_3Yb_{1.8}Cr_{0.2}Br_9$ is the most similar halide-bridged Yb^{3+}−Cr^{3+} system for which reliable exchange-coupling strengths could be found. This rough scaling reduces H_{mol} to ∼14 T. Accounting for the larger g value of Yb^{3+} (∼2.7; see the Supporting Information), our best estimate is $H_{mol} \approx 10$ T for Yb^{3+} ions within CrI_3. Future spectroscopic measurements (e.g., inelastic neutron scattering, Mössbauer, etc.) and calculations will be needed to refine this estimate, but the central conclusion drawn from both the experimental data and this analysis is clear: Yb^{3+} magnetization in Yb^{3+}:CrI_3 is effectively pinned to the magnetic ordering of the CrI_3 lattice through strong Yb^{3+}−Cr^{3+} superexchange coupling. The large H_{mol} in Yb^{3+}:CrI_3 is attributable in large part to the Yb^{3+}−I^- covalency discussed above. For comparison, exchange fields of 1.7 and ∼1.1 T are reported for Yb^{3+} in ferrimagnetic hexagonal $YbFeO_3$[40] and distorted orthorhombic $YbCrO_3$.[41] At these values, Yb^{3+} magnetization is not pinned to the ordered TM^{3+} spin sublattices.

A further remarkable aspect of Yb^{3+}:CrI_3 is that the effects of H_{mol} are evident even at zero magnetic field ($H_{ext} = 0$). Figure 4a plots zero-field Yb^{3+} PL spectra as a function of temperature from 4 to 200 K. Viewing the data starting from high temperature, the peak positions appear nearly constant until roughly T_C. Below T_C, the peaks all shift to lower energy together. This red shift is also evident in Figure 3e. Figure 4b highlights the temperature dependence of the $\Gamma_8 \rightarrow \Gamma_7$ transition energy. From 120 K to ∼T_C, the transition energy increases gradually by only ∼2 meV. Such temperature dependence has been variously modeled in terms of Raman scattering of nonresonant phonons or direct absorption/emission of phonons resonant with a crystal-field splitting.[42,43] For example, both models reproduce the $^2F_{7/2} \rightarrow {}^2F_{5/2}$ transition energies of Yb^{3+}:YAG well, whereas the resonant phonon model reproduces absorption line widths marginally better.[43] As such, we apply the resonant phonon model here. The PL energies above T_C are thus described by eq 4[42,43]

$$E(T) = E_0 + \frac{\alpha_s}{e^{\Delta/k_BT} - 1} \quad T > T_C \tag{4}$$

where E_0 is the energy at 0 K, α_s describes the electron−phonon interaction strength, and Δ is the energy of the activating phonon mode, fixed at $\Delta = 127$ cm^{-1} (15.7 meV, Figure 3b).

The solid curve in the high-temperature portion of Figure 4b (>T_C) shows a fit to the high-temperature data using eq 4, floating E_0 and α_s and yielding best-fit values of 1.1242 eV and −6.3 meV, respectively. Equation 4 plateaus at E_0 in the limit of 0 K (dashed line <T_C in Figure 4b), but the experimental peak energy shows a discontinuity at T_C, dropping sharply and decreasing with decreasing temperature until reaching ∼7 meV below E_0 in the low-temperature limit. With its link to T_C and its characteristic curvature, this trend in Yb^{3+} PL energy is associated with the spontaneous magnetization of individual CrI_3 monolayers, even though there is no net magnetization in these samples.

Spontaneous ferromagnetic ordering is classified as a second-order phase transition and, within the theory of universal scaling laws, is characterized by the order parameter β shown in eq 5 describing the magnetization temperature dependence:[44]

$$M(T) = M_0\left(-\frac{T - T_C}{T_C}\right)^{\beta} \tag{5}$$

M_0 is the saturation moment per magnetic ion and equals 3.1 μ_B for CrI_3.[18] The precise value of β depends on the underlying spin physics, but it is commonly around 1/3.[12] A previous examination of bulk CrI_3 found a critical exponent of β = 0.284, between that expected from the 3D Ising model (β = 0.325) and that of the tricritical mean-field model (β = 0.250).[34] Accordingly, the data in Figure 4b below T_C were simulated using eq 6 (sum of eqs 4 and 5, with eq 4 parameters fixed by the high-temperature data). The scaling parameter (γ) in eq 6 relates magnetization to the PL energy shift. The data are reproduced well using fixed values of $\beta = 1/3$, $T_C = 60$ K, and $\Delta = 127$ cm^{-1} (15.7 meV), with γ as the only adjustable parameter. Relating eqs 5 and 6, these results indicate an Yb^{3+} PL energy shift of −2.2 meV/μ_B during spontaneous CrI_3 intralayer magnetization. We stress that the zero-field PL data in Figure 4 are not magnetic data but highlight the strong influence of CrI_3 spontaneous magnetization on the Yb^{3+} PL. Because T_C in these samples is indistinguishable from that of bulk CrI_3 (Figure 3f and Figure S15), we tentatively attribute the small apparent broadening of the PL energy discontinuity around T_C in Figure 4b to additional PL hot bands that are not spectrally resolved.

$$E(T) = E_0 + \frac{\alpha_s}{e^{\Delta/k_BT} - 1} + \gamma\left(-\frac{T - T_C}{T_C}\right)^{\beta} \quad T < T_C \tag{6}$$

Figure 4c plots the temperature dependence of the $\Gamma_8 \rightarrow \Gamma_7$ line width (full width at half-maximum, fwhm). These data show trends similar to those observed in the peak energies of Figure 4b. Below T_C, the fwhm decreases from ∼9 to ∼4.5 meV in the low-temperature limit, attributed to the reduction in spin disorder around Yb^{3+}. These data thus also reflect

https://doi.org/10.1021/acs.nanolett.2c04533
Nano Lett. 2023, 23, 1320−1326

spontaneous magnetic ordering in monolayers of CrI_3. Although distinct low-energy shoulders are not resolved in these data, we hypothesize that the energy and line width changes below T_C both ultimately stem from loss of hot-magnon sideband intensity as CrI_3 monolayers order magnetically.[45] It will be an interesting future direction to explore magnon coupling to f−f transitions in these and related doped 2D magnetic materials.

In summary, doping Yb^{3+} into the 2D van der Waals ferromagnet CrI_3 transforms this material's PL from a broadband to a sharp multi-line, while retaining its key magnetic functionality. The f−f PL of Yb^{3+}:CrI_3 is anomalously low in energy, reflecting relatively covalent Yb^{3+}−I^- bonding. Yb^{3+} magnetization is pinned to CrI_3 by strong superexchange interactions, which contribute an effective internal field of ∼10 T that is greater than the field required for magnetic saturation of paramagnetic Yb^{3+} and much greater than the field required for full CrI_3 magnetization at low temperature (∼0.2 T). Flipping the magnetization of CrI_3 with a small external field thus also flips the Yb^{3+} magnetization and inverts its PL circular polarization. Magnetic pinning is maintained up to the T_C of CrI_3 but is rapidly lost above T_C. We further showed that the Yb^{3+} PL energy and line width both sense this internal field even at zero applied field, mapping spontaneous *intra*layer magnetic ordering below T_C despite the absence of net magnetization. Because each Yb^{3+} ion is a local lattice defect within an individual CrI_3 monolayer, we expect these induced functionalities to persist down to the monolayer, prompting future studies on exfoliated Yb^{3+}:CrI_3 and associated stacked van der Waals heterostructures and layered devices. These results demonstrate the power of designer defects to add functionality to 2D magnetic materials, enrich their fundamental physics, and create new materials of potential utility for future spin-photonics applications.

■ ASSOCIATED CONTENT

Supporting Information

The Supporting Information is available free of charge at https://pubs.acs.org/doi/10.1021/acs.nanolett.2c04533.

Additional experimental details, including sample preparation and characterization, additional variable-temperature PL data, PL polarization vs magnetic field data, excitation-power-dependence data, results from Yb^{3+} crystal-field calculations, and comparison of Yb^{3+} crystal-field barycenter energies in various lattices (PDF)

■ AUTHOR INFORMATION

Corresponding Author

Daniel R. Gamelin − *Department of Chemistry, University of Washington, Seattle, Washington 98195, United States;* orcid.org/0000-0003-2888-9916; Email: gamelin@uw.edu

Authors

Kimo Pressler − *Department of Chemistry, University of Washington, Seattle, Washington 98195, United States;* orcid.org/0000-0003-2788-1592

Thom J. Snoeren − *Department of Chemistry, University of Washington, Seattle, Washington 98195, United States;* orcid.org/0000-0001-8055-3710

Kelly M. Walsh − *Department of Chemistry, University of Washington, Seattle, Washington 98195, United States;* orcid.org/0000-0001-5349-8816

Complete contact information is available at: https://pubs.acs.org/10.1021/acs.nanolett.2c04533

Notes

The authors declare no competing financial interest.

■ ACKNOWLEDGMENTS

Support of this project by the US NSF (DMR-1807394) is gratefully acknowledged. Initial stages of this work were performed as part of Programmable Quantum Materials, an Energy Frontier Research Center funded by the U.S. Department of Energy (DOE), Office of Science, Basic Energy Sciences (BES), under award DESC0019443. Additional support was received from the UW Clean Energy Institute (graduate fellowships to T.J.S. and K.M.W.). Part of this work was conducted at the Molecular Analysis Facility, a National Nanotechnology Coordinated Infrastructure (NNCI) site at the University of Washington that is supported in part by the National Science Foundation (NNCI-1542101 and NNCI-2025489), the University of Washington, the Molecular Engineering & Sciences Institute, the Clean Energy Institute, and the National Institutes of Health. The authors thank Dr. Werner Kaminsky and Paige M. Gannon for single-crystal XRD measurements, Dr. Xi Wang for assistance with optical microscope measurements, Prof. Jiun-Haw Chu and Dr. Zhaoyu Liu for VSM measurements, and Prof. Robert Glaum, Maximilian Jähnig, and Julia Spitz for provision of and assistance with the BonnMag code.

■ REFERENCES

(1) Cox, P. A. *Electronic Structure and Chemistry of Solids*; Oxford University Press: 1987.

(2) Henderson, B.; Imbusch, G. F. *Optical Spectroscopy of Inorganic Solids*; Oxford University Press: 1989.

(3) Kittel, C. *Introduction to Solid State Physics*, 8th ed.; Wiley: 2004.

(4) Bassett, L. C.; Alkauskas, A.; Exarhos, A. L.; Fu, K.-M. C. Quantum defects by design. *Nanophotonics* **2019**, *8*, 1867−1888.

(5) Tran, T. T.; Elbadawi, C.; Totonjian, D.; Lobo, C. J.; Grosso, G.; Moon, H.; Englund, D. R.; Ford, M. J.; Aharonovich, I.; Toth, M. Robust Multicolor Single Photon Emission from Point Defects in Hexagonal Boron Nitride. *ACS Nano* **2016**, *10*, 7331−7338.

(6) Hong, J.; Jin, C.; Yuan, J.; Zhang, Z. Atomic Defects in Two-Dimensional Materials: From Single-Atom Spectroscopy to Functionalities in Opto-/Electronics, Nanomagnetism, and Catalysis. *Adv. Mater.* **2017**, *29*, 1606434.

(7) Cowley, R. A.; Buyers, W. J. L. The Properties of Defects in Magnetic Insulators. *Rev. Mod. Phys.* **1972**, *44*, 406−450.

(8) Wiesendanger, R. Nanoscale Magnetic Skyrmions in Metallic Films and Multilayers: A New Twist for Spintronics. *Nat. Rev. Mater.* **2016**, *1*, 16044.

(9) Lima Fernandes, I.; Bouaziz, J.; Blügel, S.; Lounis, S. Universality of Defect-Skyrmion Interaction Profiles. *Nat. Commun.* **2018**, *9*, 4395.

(10) Song, T.; Cai, X.; Tu, M. W.-Y.; Zhang, X.; Huang, B.; Wilson, N. P.; Seyler, K. L.; Zhu, L.; Taniguchi, T.; Watanabe, K.; McGuire, M. A.; Cobden, D. H.; Xiao, D.; Yao, W.; Xu, X. Giant Tunneling Magnetoresistance in Spin-Filter van der Waals Heterostructures. *Science* **2018**, *360*, 1214−1218.

(11) Huang, B.; McGuire, M. A.; May, A. F.; Xiao, D.; Jarillo-Herrero, P.; Xu, X. Emergent Phenomena and Proximity Effects in Two-Dimensional Magnets and Heterostructures. *Nat. Mater.* **2020**, *19*, 1276−1289.

(12) Gibertini, M.; Koperski, M.; Morpurgo, A. F.; Novoselov, K. S. Magnetic 2D materials and heterostructures. *Nat. Nanotechnol.* **2019**, *14*, 408−419.
(13) Gong, C.; Zhang, X. Two-dimensional magnetic crystals and emergent heterostructure devices. *Science* **2019**, *363*, No. eaav4450.
(14) Wang, Q. H.; Bedoya-Pinto, A.; Blei, M.; Dismukes, A. H.; Hamo, A.; Jenkins, S.; Koperski, M.; Liu, Y.; Sun, Q.-C.; Telford, E. J.; Kim, H. H.; Augustin, M.; Vool, U.; Yin, J.-X.; Li, L. H.; Falin, A.; Dean, C. R.; Casanova, F.; Evans, R. F. L.; Chshiev, M.; Mishchenko, A.; Petrovic, C.; He, R.; Zhao, L.; Tsen, A. W.; Gerardot, B. D.; Brotons-Gisbert, M.; Guguchia, Z.; Roy, X.; Tongay, S.; Wang, Z.; Hasan, M. Z.; Wrachtrup, J.; Yacoby, A.; Fert, A.; Parkin, S.; Novoselov, K. S.; Dai, P.; Balicas, L.; Santos, E. J. G. The Magnetic Genome of Two-Dimensional van der Waals Materials. *ACS Nano* **2022**, *16*, 6960−7079.
(15) Huang, B.; Clark, G.; Navarro-Moratalla, E.; Klein, D. R.; Cheng, R.; Seyler, K. L.; Zhong, D.; Schmidgall, E.; McGuire, M. A.; Cobden, D. H.; Yao, W.; Xiao, D.; Jarillo-Herrero, P.; Xu, X. Layer-Dependent Ferromagnetism in a van der Waals Crystal Down to the Monolayer Limit. *Nature* **2017**, *546*, 270−273.
(16) Sivadas, N.; Okamoto, S.; Xu, X.; Fennie, C. J.; Xiao, D. Stacking-Dependent Magnetism in Bilayer CrI_3. *Nano Lett.* **2018**, *18*, 7658−7664.
(17) Seyler, K. L.; Zhong, D.; Huang, B.; Linpeng, X.; Wilson, N. P.; Taniguchi, T.; Watanabe, K.; Yao, W.; Xiao, D.; McGuire, M. A.; Fu, K.-M. C.; Xu, X. Valley Manipulation by Optically Tuning the Magnetic Proximity Effect in WSe_2/CrI_3 Heterostructures. *Nano Lett.* **2018**, *18*, 3823−3828.
(18) McGuire, M. A.; Dixit, H.; Cooper, V. R.; Sales, B. C. Coupling of Crystal Structure and Magnetism in the Layered, Ferromagnetic Insulator CrI_3. *Chem. Mater.* **2015**, *27*, 612−620.
(19) Dillon, J. F.; Kamimura, H.; Remeika, J. P. Magneto-Optical Properties of Ferromagnetic Chromium Trihalides. *J. Phys. Chem. Solids* **1966**, *27*, 1531−1549.
(20) Suits, J. Faraday and Kerr Effects in Magnetic Compounds. *IEEE Trans. Magn.* **1972**, *8*, 95−105.
(21) Güdel, H. U.; Snellgrove, T. R. Jahn-Teller Effect in the $^4T_{2g}$ State of Chromium(III) in Dicesium Sodium Indium(III) Hexachloride. *Inorg. Chem.* **1978**, *17*, 1617−1620.
(22) Peng, B.; Chen, Z.; Li, Y.; Liu, Z.; Liang, D.; Deng, L. Multiwavelength Magnetic Coding of Helical Luminescence in Ferromagnetic 2D Layered CrI_3. *iScience* **2022**, *25*, 103623.
(23) Wyart, J.-F.; Tchang-Brillet, W.-Ü. L.; Spector, N.; Palmeri, P.; Quinet, P.; Biémont, E. Extended Analysis of the Spectrum of Triply-ionized Ytterbium (Yb IV) and Transition Probabilities. *Phys. Scr.* **2001**, *63*, 113−121.
(24) Georgescu, A. B.; Millis, A. J.; Rondinelli, J. M. Trigonal Symmetry Breaking and Its Electronic Effects in the Two-Dimensional Dihalides MX_2 and Trihalides MX_3. *Phys. Rev. B* **2022**, *105*, 245153.
(25) Bronova, A.; Bredow, T.; Glaum, R.; Riley, M. J.; Urland, W. BonnMag: Computer Program for Ligand-Field Analysis of f^n Systems Within the Angular Overlap Model. *J. Comput. Chem.* **2018**, *39*, 176−186.
(26) Zhang, Y.; Wu, X.; Lyu, B.; Wu, M.; Zhao, S.; Chen, J.; Jia, M.; Zhang, C.; Wang, L.; Wang, X.; Chen, Y.; Mei, J.; Taniguchi, T.; Watanabe, K.; Yan, H.; Liu, Q.; Huang, L.; Zhao, Y.; Huang, M. Magnetic Order-Induced Polarization Anomaly of Raman Scattering in 2D Magnet CrI_3. *Nano Lett.* **2020**, *20*, 729−734.
(27) Al-Mobarak, R.; Warren, K. D. The Effect of Covalency on the Spin—Orbit Coupling Constant. *Chem. Phys. Lett.* **1973**, *21*, 513−516.
(28) Bungenstock, C.; Tröster, T.; Holzapfel, W. B. Effect of Pressure on Free-Ion and Crystal-Field Parameters of Pr^{3+} in LOCl (L = La, Pr, Gd). *Phys. Rev. B* **2000**, *62*, 7945−7955.
(29) Schwartz, R. W. Electronic Structure of the Octahedral Hexachloroytterbate Ion. *Inorg. Chem.* **1977**, *16*, 1694−1698.
(30) Kanellakopulos, B.; Amberger, H. D.; Rosenbauer, G. G.; Fischer, R. D. Zur Elektronenstruktur hochsymmetrischer Verbindungen der Lanthanoiden und Actinoiden—V: Paramagnetische Suszeptibilität und elektronisches Raman-Spektrum von Cs_2NaYb-(III)Cl_6. *J. Inorg. Nucl. Chem.* **1977**, *39*, 607−611.
(31) Tsujii, N.; Imanaka, Y.; Takamasu, T.; Kitazawa, H.; Kido, G. Photoluminescence of Yb^{3+}-Doped $CuInS_2$ Crystals in Magnetic Fields. *J. Appl. Phys.* **2001**, *89*, 2706−2710.
(32) Haumesser, P.-H.; Gaumé, R.; Viana, B.; Antic-Fidancev, E.; Vivien, D. Spectroscopic and Crystal-Field Analysis of New Yb-doped Laser Materials. *J. Phys.: Cond. Mater.* **2001**, *13*, 5427−5447.
(33) de Maat-Gersdorf, I. *Spectroscopic Analysis of Erbium-Doped Silicon and Ytterbium Doped Indium Phosphide*; University of Amsterdam: 2001.
(34) Liu, Y.; Petrovic, C. Three-Dimensional Magnetic Critical Behavior in CrI_3. *Phys. Rev. B* **2018**, *97*, 014420.
(35) Coey, J. M. D. *Magnetism and Magnetic Materials*; Cambridge University Press: 2010.
(36) Lado, J. L.; Fernández-Rossier, J. On the Origin of Magnetic Anisotropy in Two Dimensional CrI_3. *2D Mater.* **2017**, *4*, 035002.
(37) Aebersold, M. A.; Güdel, H. U.; Hauser, A.; Furrer, A.; Blank, H.; Kahn, R. Exchange Interactions in Mixed Yb^{3+}-Cr^{3+} and Yb^{3+}-Ho^{3+} Dimers: An Inelastic-Neutron-Scattering Investigation of $Cs_3Yb_{1.8}Cr_{0.2}Br_9$ and $Cs_3Yb_{1.8}Ho_{0.2}Br_9$. *Phys. Rev. B* **1993**, *48*, 12723−12731.
(38) Mironov, V. S.; Chibotaru, L. F.; Ceulemans, A. Exchange Interaction in the $YbCrBr_9^{3-}$ Mixed Dimer: The Origin of a Strong Yb^{3+}-Cr^{3+} Exchange Anisotropy. *Phys. Rev. B* **2003**, *67*, 014424.
(39) Atanasov, M.; Daul, C.; Güdel, H. U. Modelling of Anisotropic Exchange Coupling in Rare-Earth -Transition-Metal Pairs: Applications to Yb^{3+}-Mn^{2+} and Yb^{3+}-Cr^{3+} Halide Clusters and Implications to the Light Up-Conversion. *Comp. Chem.: Rev. Current Trends* **2005**, *9*, 153−194.
(40) Cao, S.; Sinha, K.; Zhang, X.; Zhang, X.; Wang, X.; Yin, Y.; N'Diaye, A. T.; Wang, J.; Keavney, D. J.; Paudel, T. R.; Liu, Y.; Cheng, X.; Tsymbal, E. Y.; Dowben, P. A.; Xu, X. Electronic Structure and Direct Observation of Ferrimagnetism in Multiferroic Hexagonal $YbFeO_3$. *Phys. Rev. B* **2017**, *95*, 224428.
(41) Dalal, B.; Sarkar, B.; Dev Ashok, V.; De, S. K. Evolution of Magnetic Properties and Exchange Interactions in Ru Doped $YbCrO_3$. *J. Phys.: Cond. Mater.* **2016**, *28*, 426001.
(42) Imbusch, G. F.; Yen, W. M.; Schawlow, A. L.; McCumber, D. E.; Sturge, M. D. Temperature Dependence of the Width and Position of the $^2E \rightarrow {}^4A_2$ Fluorescence Lines of Cr^{3+} and V^{2+} in MgO. *Phys. Rev.* **1964**, *133*, A1029−A1034.
(43) Böttger, T.; Thiel, C. W.; Cone, R. L.; Sun, Y.; Faraon, A. Optical Spectroscopy and Decoherence Studies of Yb^{3+}:YAG at 968 nm. *Phys. Rev. B* **2016**, *94*, 045134.
(44) Fisher, M. E. The Theory of Equilibrium Critical Phenomena. *Rep. Prog. Phys.* **1967**, *30*, 615−730.
(45) Bermudez, V. M.; McClure, D. S. Spectroscopic studies of the two-dimensional magnetic insulators chromium trichloride and chromium tribromide—II. *J. Phys. Chem. Solids* **1979**, *40*, 149−173.

https://doi.org/10.1021/acs.nanolett.2c04533
Nano Lett. 2023, 23, 1320−1326